Chapter 17. Rainfall

Werner Alpers
Institut für Meereskunde, Universität Hamburg, Hamburg, Germany

Christian Melsheimer[1]
Centre for Remote Imaging, Sensing and Processing, National University of Singapore, Singapore

17.1 Introduction

Rainfall is one of the most important atmospheric phenomena. It has a strong impact on the global-scale atmospheric circulation as well as on local weather. Of the heat energy that the global atmosphere receives (and that balances its net radiative energy loss), about 70 to 85 percent is latent heat released by the formation of precipitation [*Simpson et al.*, 1996; *Barry* and *Chorley*, 1987; *Salby*, 1996].

Rain can occur as stratiform rain or convective rain (rain cells). Stratiform rain is the dominant from of rain in the high latitudes, while convective rain is the dominant form of rain in the tropics and subtropics (in the tropics, 50 to 80 percent of the precipitation is convective rain) [*Houze,* 1997]. However, even on synthetic aperture radar (SAR) images acquired by the European Remote Sensing satellites ERS-1 and ERS-2 over the Greenland Sea, strong rain cells have been repeatedly identified. Rain cells typically have diameters between 5 km and 10 km and duration of about 10 to 30 min, and can occur singly or in clusters. Occasionally, so-called supercells with diameters exceeding 70 km have been observed. Stratiform rain is generally much less intense, but it lasts longer than convective rain. In general, stratiform rain is too weak and too uniform spatially to be visible in SAR images of the sea. Thus, it is mainly convective rain in the form of rain cells that is observed in SAR images.

Currently, the only feasible way to measure the distribution of rainfall on a global scale is by satellite remote sensing techniques. Spaceborne instruments capable of yielding information about rainfall include the Special Sensor Microwave Imager (SSM/I) aboard the U.S. Defense Meteorological Satellite Program (DMSP) satellites, the microwave instrument (TMI), the precipitation radar (PR) flying aboard the U.S.-Japanese Tropical Rainfall Measuring Mission (TRMM) satellite [*Simpson et al.*, 1996; *Kummerow et al.*, 1998] and the altimeters operating at different microwave frequencies aboard the U.S.-French TOPEX/Poseidon and Jason satellites [*Tournadre* and *Morland*, 1997]. All these spaceborne instruments have relatively coarse spatial resolution (the best is the PR aboard the TRMM satellite which has a footprint of 4 km) and thus cannot resolve individual rain cells that often have an extent of only a few kilometers. All the above-mentioned instruments yield rain information by means of scattering or attenuation of microwaves by rain drops in the atmosphere. Information on the rain cell geometry can also be extracted from the distortion of the leading edge of the return pulse of a radar altimeter as shown by *Tournadre* [1998].

Since at least the time of the SEASAT mission in 1978, it has been noticed that footprints of rain cells can also be detected on radar images of the sea surface [*Fu and Holt*, 1982; *Atlas*, 1994a; *Atlas and Black*, 1994; *Iguchi et al.*, 1995; *Lichtenegger*, 1996; *Jameson et al.*, 1997; *Moore et al.*, 1997; *Melsheimer et al.*, 1998, 2001; *Lin et al.*, 2001]. These observations have

---

[1] now at: Institut für Umweltphysik, Universitaet Bremen, Bremen Germany

opened up the possibility to measure the distribution of rain events over the ocean with high horizontal resolution (10 m to 100 m) on a global scale. However, how to extract the best rainfall rates from these radar images continues to be a research topic.

17.2 Radar Signatures of Rain Cells

Radar signatures of rain in SAR images acquired over the ocean are caused by (1) radar backscattering from the sea surface (surface scattering) and (2) by scattering and attenuation of the microwaves by rain drops (or hydrometeors) in the atmosphere (volume scattering and attenuation).

The radar backscattering from the rough sea surface at incident angles (where incident angle is the angle between nadir and the radar beam) between 20° and 70° can be described by the so-called Bragg scattering theory [*Valenzuela*, 1978]. The power of the radar backscatter from the sea surface is proportional to the power spectral density of those water waves which propagate towards or away from the look direction of the radar antenna and which have a wavelength, λ_B, of $\lambda_B = \lambda_0/2\sin\theta$, where λ_0 denotes the radar wavelength and θ denotes the incident angle of the radar beam. The wavelength, λ_B, is called the Bragg wavelength. The power spectral density (or the amplitude squared) of the Bragg waves is modified by rain via two effects that modify the sea surface roughness: (1) rain drops impinging onto the sea surface and (2) the wind gusts or downdrafts associated with rain cells.

17.2.1 Rainfall Effects on the Sea Surface

Raindrops impinging on the sea surface generate ring waves which enhance the sea surface roughness [*Moore et al.*, 1979; *Bliven et al.*, 1997; *Craeye et al.*, 1997], and also generate turbulence in the upper water layer which attenuates the short surface waves [*Nystuen*, 1990; *Tsimplis*, 1992]. Analyses of multifrequency data from the Spaceborne Imaging Radar C/X-band SAR (SIR-C/X-SAR) mission in 1994 acquired over ocean areas [*Melsheimer et al.*, 1998] and laboratory measurements at a wind wave tank [*Braun et al.*, 2002] have shown that the modification of the sea surface roughness by impinging rain drops depends strongly on the wavelength of the water waves. The net effect of impinging rain drops on the sea surface is a decrease in amplitude of water waves with wavelengths above 10 cm and an increase in amplitude of water waves with wavelengths below 5 cm. The critical wavelength at which impinging rain drops cause an increase of the wave amplitude rather than a decrease is not well defined. The critical wavelength depends on rain rate, drop size distribution, wind speed, and temporal evolution of the rain event. At the initial stage of the rain event, the turbulence in the upper water layer is not fully developed and thus its damping effect on the water waves is small. On the other hand, after it has stopped raining, the turbulence does not decay immediately (the lifetime of the turbulence is on the order of one minute) and it keeps damping the waves even after the rain event has ended. The Bragg wavelength of the ERS SAR (radar frequency: 5.3 GHz, C-band, incident angle 19° to 26°) lies between 8.2 cm and 6.5 cm. Unfortunately, these wavelengths lie in the transition region where, depending on the rain rate, the drop size distribution, the wind speed, and the time history of the rain event, the impinging rain drops can give rise to either an increase or a decrease in the amplitude of the Bragg waves and, thus, to an increase or a decrease of the backscattered radar power. These factors often make it difficult to unambiguously identify rain events on ERS SAR images acquired over the ocean. For higher and lower radar frequencies, the situation is much more clear-cut: X-band Bragg waves (X-band

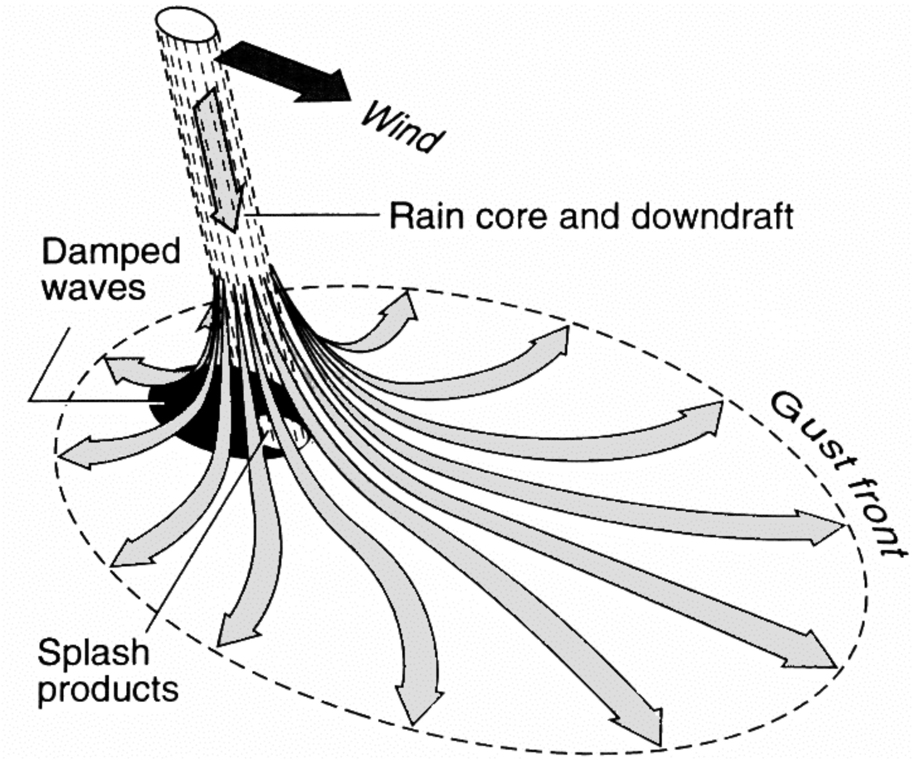

Figure 17.1. Schematic sketch of the downdraft associated with a rain cell. The downdraft spreads over the sea surface, causing and enhanced roughening of the sea surface and, thus, an increase in the backscattered radar power [After *Atlas*, 1994b].

frequency: 8.5 to 12.5 GHz) are generally enhanced by impinging rain, and L-band Bragg waves (L-band frequency is 1 to 2 GHz) are usually damped by rain, although some exceptions have been reported [*Atlas*, 1994a].

17.2.2 Rain-related Wind Effects on the Sea Surface

In general, rain events are associated with wind gusts that roughen the sea surface. Precipitation from a rain cell usually produces a downward airflow, called a downdraft, by entrainment and by evaporative cooling under the cloud [e.g., *Cotton and Anthes*, 1989]. When the downdraft reaches the sea surface, it spreads radially outward as a strong local surface wind, thereby causing an increase in sea surface roughness.

The airflow pattern caused by the downdraft of a rain cell is shown schematically in Figure 17.1. The outer edge of this radially-spreading downdraft is called a gust front. If the ambient wind field is weak and does not disturb this airflow pattern, the radially-spreading downdraft is visible on SAR images of the sea surface as a nearly circular bright pattern with a sharp edge [*Atlas*, 1994a; 1994b]. Such a pattern is usually less bright in the center, where the downdraft reaches the ground and horizontal wind speeds are lowest. The lower the ambient wind speed, the higher is the contrast between the bright pattern and the surroundings. Therefore, radar signatures of rain cells are often more pronounced over tropical oceans where low wind speeds prevail.

When a strong ambient wind field is present, the radially-symmetric spreading downdraft is distorted and likewise is the resulting radar signature. In the case of a strong ambient wind field, the downwind side of the rain cell is imaged brighter and the upwind side darker than the surrounding area. The brightness increases downwind as the horizontal wind vectors of the radially-spreading downdraft add positively to the ambient wind vector; the brightness decreases upwind as the two vectors add negatively.

Another effect that, in principle, contributes to the asymmetry of radar signatures of downdrafts is the dependence of the radar backscattering on azimuth angle, i.e.; on the angle between the wind direction and the radar look direction. However, simulations of open convective cells [*Mitnik*, 1992] have shown that the dominant factors determining the shape and orientation of radar signatures of convective cells are the direction of the ambient (or background) wind and the ratio between the speed of the ambient wind and the speed of the horizontally-spreading radial wind associated with the convective cell. Furthermore, in the case of rain cells with little or no ambient wind, the contrast between the mean backscatter level inside and outside the area of the radially-spreading downdraft is usually much larger than the variation of the radar backscatter caused by the changing wind direction relative to the radar look direction (variation in azimuth direction). Therefore, in practically all radar images of the sea surface that show radar signatures of rain cells, little or no variation of contrast with azimuth angle is observed. Thus, a typical radar signature of a radially-spreading downdraft associated with a rain cell is a circular or elliptical pattern that is either (1) brighter than the surrounding area, or (2) brighter than the surrounding area on one side (the downwind side) and darker on the opposite side (the upwind side).

The radar signature of the radially-spreading downdraft associated with a rain cell is expected to look qualitatively the same at all radar frequencies, since increased wind speed increases the amplitude of the Bragg waves for all radar wavelengths and reduced wind speed decreases the amplitude of the Bragg waves. The response or relaxation time (i.e., the time it takes for the waves to build up once the wind starts blowing, or the time it takes for the waves to react to changes in wind speed and direction) is longer for longer waves, but in the case of Bragg waves having wavelengths between 3 cm and 30 cm, this relaxation time is at most on the order of seconds to tens of seconds.

17.2.3 Scattering and Attenuation of Microwaves by Rain Drops in the Atmosphere

Microwaves are also scattered and attenuated by raindrops in the atmosphere, or more precisely, by hydrometeors—which, in addition to rain, include frozen water particles such as ice crystals, frozen drops or clusters thereof. The effect of hydrometeors is called volume scattering and volume attenuation and has been studied extensively by radar meteorologists, who use weather radars for measuring rainfall [e.g., *Doviak and Zrnic*, 1993; *Sauvageot*, 1991]. Both volume scattering and volume attenuation are strong functions of radar frequency and rain rate. The higher the radar frequency and the rainfall rate, the stronger are the microwaves scattered and attenuated by hydrometeors. At a radar frequency of 10 GHz (X-band), the attenuation by hydrometeors can be quite strong—as evidenced by X-band SAR images acquired over the rainforest by the X-band SAR aboard the spaceshuttle Endeavor during the Spaceborne Imaging Radar C/X-SAR (SIR-C/X-SAR) mission in 1994 [*Jameson et al.*, 1997; *Melsheimer et al.*, 1998]. Figure 17.2, acquired over the rainforest near Manaus, Brazil, is an example of an image showing the effect of radar frequency and rain rate on volume scattering and volume attenuation. It shows on the X-band image a dark area in the lower right-hand section (caused by the attenuation), but nothing similar in this area on the L-band image.

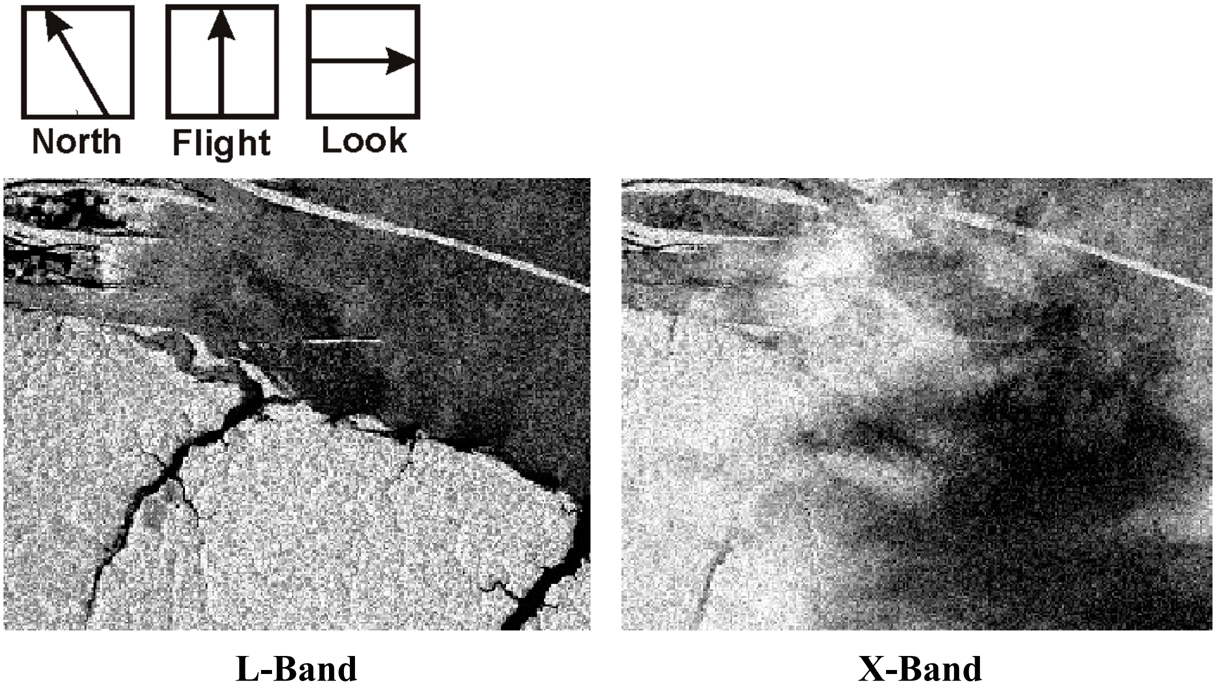

Figure 17.2. SIR-C/X-SAR images acquired on 16 April 1994 at 0548 UTC (Data take 110.5) over the Brazilian rain forest near Manaus. Visible are the rainforest (lower left-hand section) and the river Rio Negro (upper right-hand section). The two images were acquired simultaneously at L-band (left) and X-band (right) and both at VV polarization. The dark area in the lower right-hand section of the X-band image is caused by raindrops in the atmosphere, which attenuate the X-band microwaves. Each imaged area is approximately 16 km × 12 km, center location 1°30'S, 48°54'W

Backscattering of microwaves by hydrometeors, sometimes called rain echo, is sometimes visible on X-band radar images acquired over uniform land areas, where the echoes show up as (slightly) bright patches. Because of the SAR imaging geometry, the bright patches are shifted in the radar image towards near range with respect to the position of the rain cell over the surface [*Melsheimer et al.*, 1998]. The X-band SAR image depicted in Figure 17.3 was, like the image depicted in Figure 17.2, acquired over the Brazilian rain forest during the SIR-C/X-SAR mission in 1994. It shows X-band radar signatures of rain cells over dense and uniform vegetation. The radar signatures consist of (1) (slightly) bright patches caused by the backscattering of the microwaves by hydrometeors and (2) adjacent dark shadows caused by the attenuation of the microwaves by hydrometeors. However, on X-band SAR images acquired over ocean areas, the bright radar echoes caused by scattering at hydrometeors are usually not detectable, because rain-induced effects are dominant. The bright patches that are sometimes visible on X-band radar images of rain cells over the ocean are, very likely, almost always due to rain-induced enhancement of the amplitude of X-band Bragg waves. This is inferred because, on simultaneously acquired L- and X-band images, the L-band images usually show dark areas (caused by rain-induced damping of L-band Bragg waves) where the X-band images show bright areas [e.g., *Melsheimer et al.*, 1998].

At 5.3 GHz (C-band), the radar frequency at which the SARs aboard the satellites ERS-1, ERS-2, RADARSAT-1, ENVISAT, and RADARSAT-2 operate, the scattering and attenuation by rain drops in the atmosphere are usually small and can be neglected. But there are exceptions: if the rain rate is above 50 mm/hour, the attenuation becomes significant and, if the rate is above

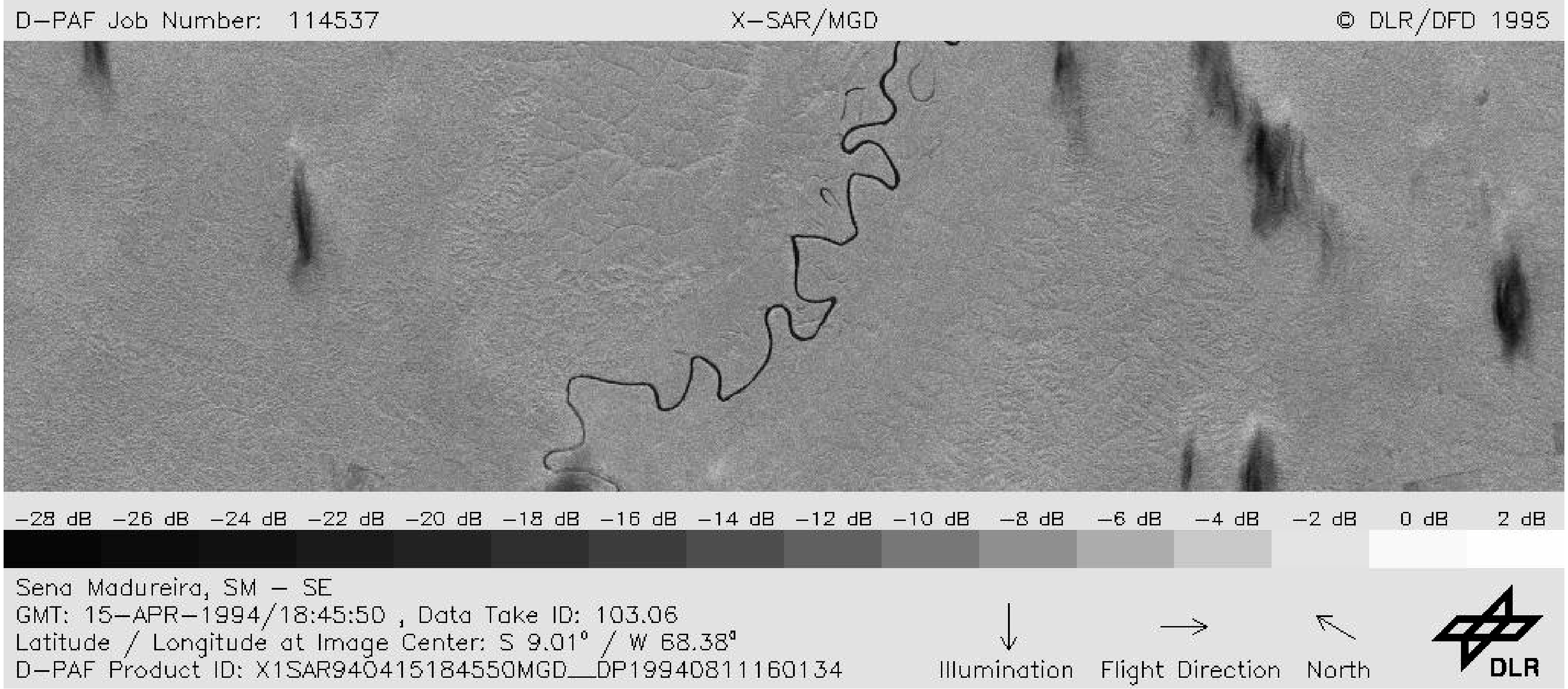

Figure 17.3. SIR-C/X-SAR image acquired on 15 April 1994 at 1845 UTC over dense vegetation in Brazil (Data take103.6) at X-band, VV polarization. The image shows several "shadows" of rain cells. The shadows are due to attenuation of microwaves by raindrops in the atmosphere. Several of the shadows are accompanied by adjacent, slightly bright patches on their near-range side (at top in the image), due to backscattering of microwaves by raindrops in the atmosphere. The imaged area is approximately 100 km x 14 km, center location 9°01'S, 68°23'W.

100 mm/hour, it even can become the dominant effect [*Lin et al*, 2001]. At lower radar frequencies, e.g., at L-band, volume scattering and attenuation by raindrops in the atmosphere is negligible.

17.3 Examples of SAR images showing radar signatures of rain cells

The SAR images showing radar signatures of rain cells presented in this section were mainly acquired by the C-band SAR aboard the European Remote Sensing satellites, ERS-1 and ERS-2. A few examples of SAR images are also shown that were acquired simultaneously at different radar frequencies and polarizations during the SIR-C/X-SAR missions in 1994. The SAR of the ERS satellites operates at a frequency of 5.3 GHz at VV polarization, whereas the SIR-C/X-SAR instrument was capable of operating simultaneously at frequencies of 1.25 GHz (L-band), 5.3 GHz (C-band) and 9.6 GHz (X-band). At L- and C-band, multi-polarization images (at HH, VV, and HV polarizations) could be taken.

Figures 17.4, 17.5, 17.6 and 17.8 are examples of radar images depicting radar signatures of rain cells with strong signatures of the radially-spreading downdraft. Figure 17.4 shows an ERS-1 SAR image acquired on 3 April 1996, 1234 UTC over the Andaman Sea west of the Nicobar islands during calm wind conditions. The circular bright patterns with a dark “hole” in the center are sea surface manifestations of tropical rain cells. The circular bright area depicts the radially-spreading downdraft. Arrow 1 inserted into Figure 17.4 indicates the gust front associated with the rain cell and arrow 2 indicates the ocean surface area where the Bragg waves are strongly damped by the turbulence generated by rain drops impinging onto the sea surface. Also visible are sea surface manifestations of packets of internal solitary waves (see Chapter 7 for a discussion of internal waves).

Figure 17.5 is an ERS-1 SAR image acquired on 18 April 1994, 0342 UTC over the Gulf of Thailand showing a cluster of rain cells. The inserted arrows labeled “1” point to the gust fronts and the arrows labeled “2” point to the areas where the Bragg waves are strongly damped by the turbulence generated by heavy rainfall. Figure 17.6 depicts an ERS-1 SAR image acquired on 18 April 1994, 0342 UTC over the Gulf of Thailand (adjacent to the previous image) and shows a string of rain cells with decreasing diameters (marked "1" to "6"). Signature 1 is a typical almost circular pattern caused by the radially-spreading downdraft (diameter in this case is about 20 km). The dark patch in the center is the radar signature of impinging rain (diameter in this case is about 3 km). The six rain cells are very likely at different stages of their life cycles. The more time that has elapsed since the downdraft first reached the sea surface, the larger is the diameter of the downdraft pattern. Thus rain cell 1 should be the oldest, and rain cell 6 the youngest. Note also the mottled texture in the lower right-hand section of Figure 17.5 and in the upper right-hand section of Figure 17.6. This texture is caused by atmospheric convective cells as discussed in Chapter 14.

Figure 17.7 shows an ERS-2 SAR image acquired on 15 December 1999, 0226 UTC over the Sulu Sea near Palawan Island (Philippines). Several small-scale rain cells located at or near an atmospheric front are visible. This is a typical example for rain cells without a pronounced downdraft pattern. Only irregular and rather small bright and dark patches caused by the enhancement and reduction of the amplitude of the Bragg waves by impinging raindrops are visible on this radar image.

Figure 17.8 shows an ERS-1 SAR image, acquired on 7 November 1996, 1223 UTC over the southern coast of Iceland. The circular pattern is caused by the radially spreading downdraft. Near the center of this circular pattern, slightly darker patches indicate the area where Bragg

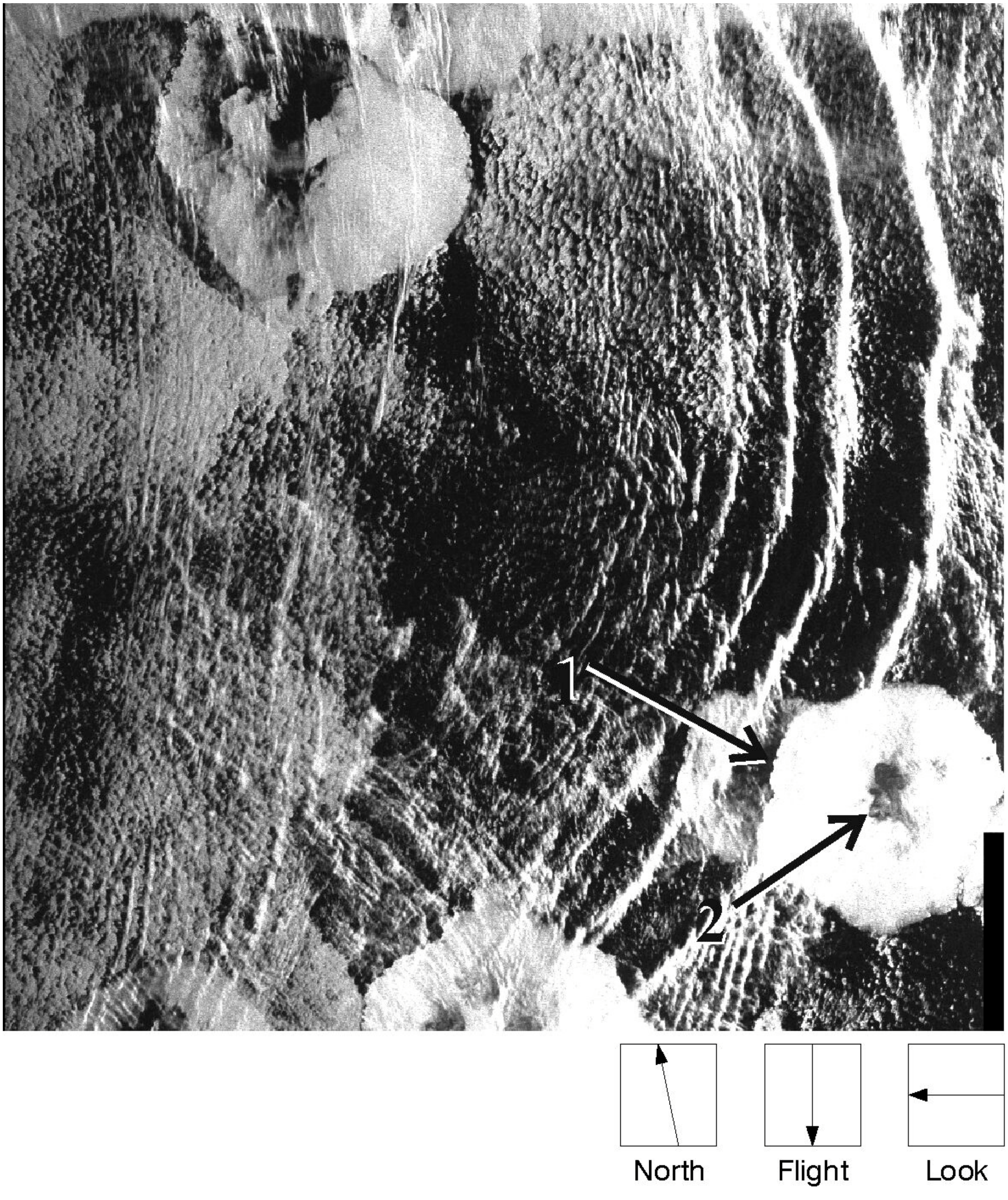

Figure 17.4. ERS-1 (C-band, VV) SAR image acquired on 03 April 1996, 1234 UTC over the Andaman Sea (orbit 24684, frame 3429), showing strong circular rain cells. Arrow “1” points at the gust front of a rain cell and arrow “2” points at a dark area where rain-induced turbulence dampens the Bragg waves. The imaged area is approximately 100 km × 100 km, center location 8°48’N, 94°56’E. ©ESA 1996

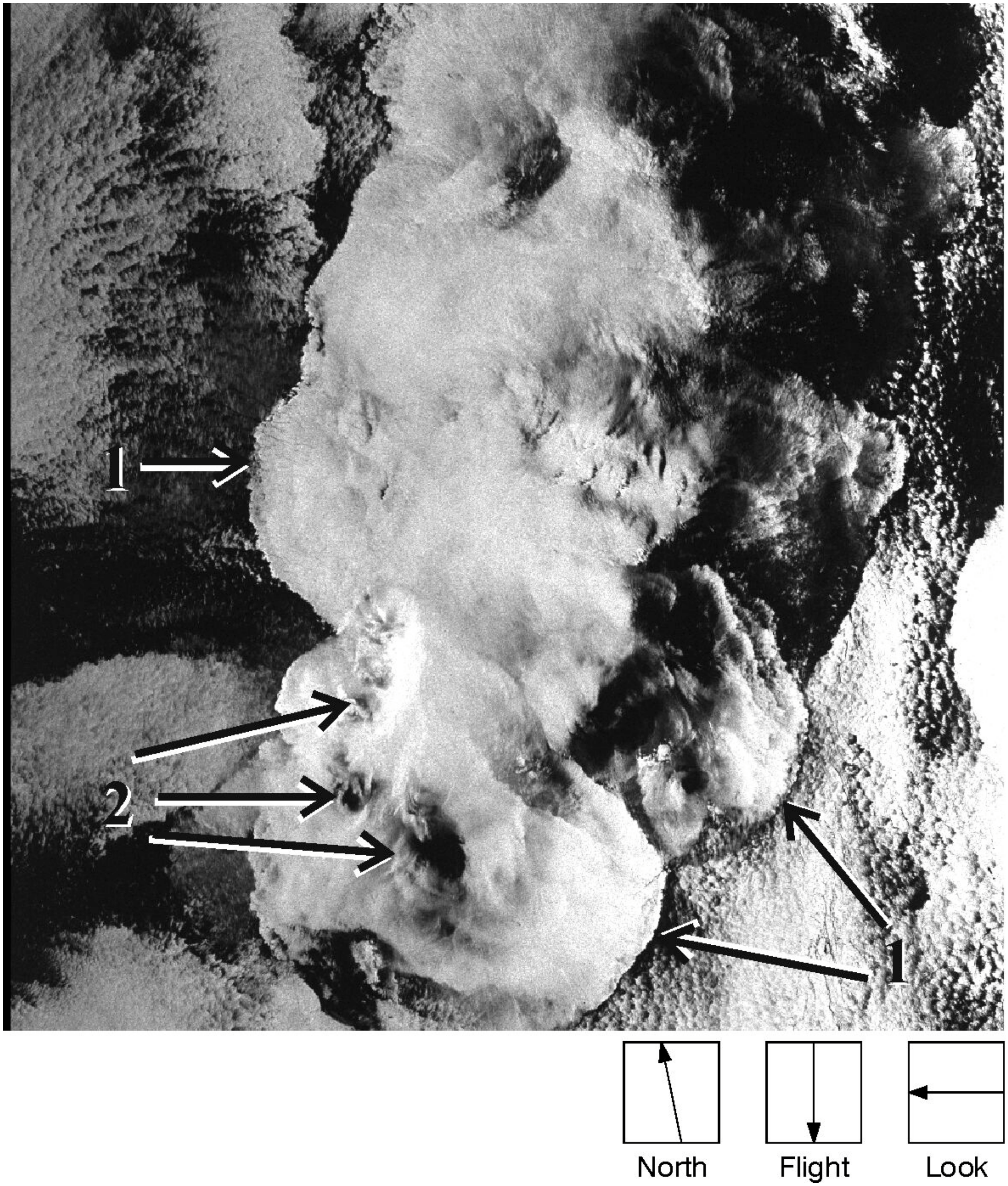

Figure 17.5. ERS-1 (C-band, VV) SAR image acquired on 18 April 1994, 0342 UTC over the Gulf of Thailand (orbit 14408, frame 3411), showing a cluster of rain cells. The arrows "1" point at the gust fronts of rain cells and the arrows "2" point at dark areas where rain-induced turbulence dampens the Bragg waves. The imaged area is approximately 100 km × 100 km, center location 9°41'N, 100°35'E. ©ESA 1994

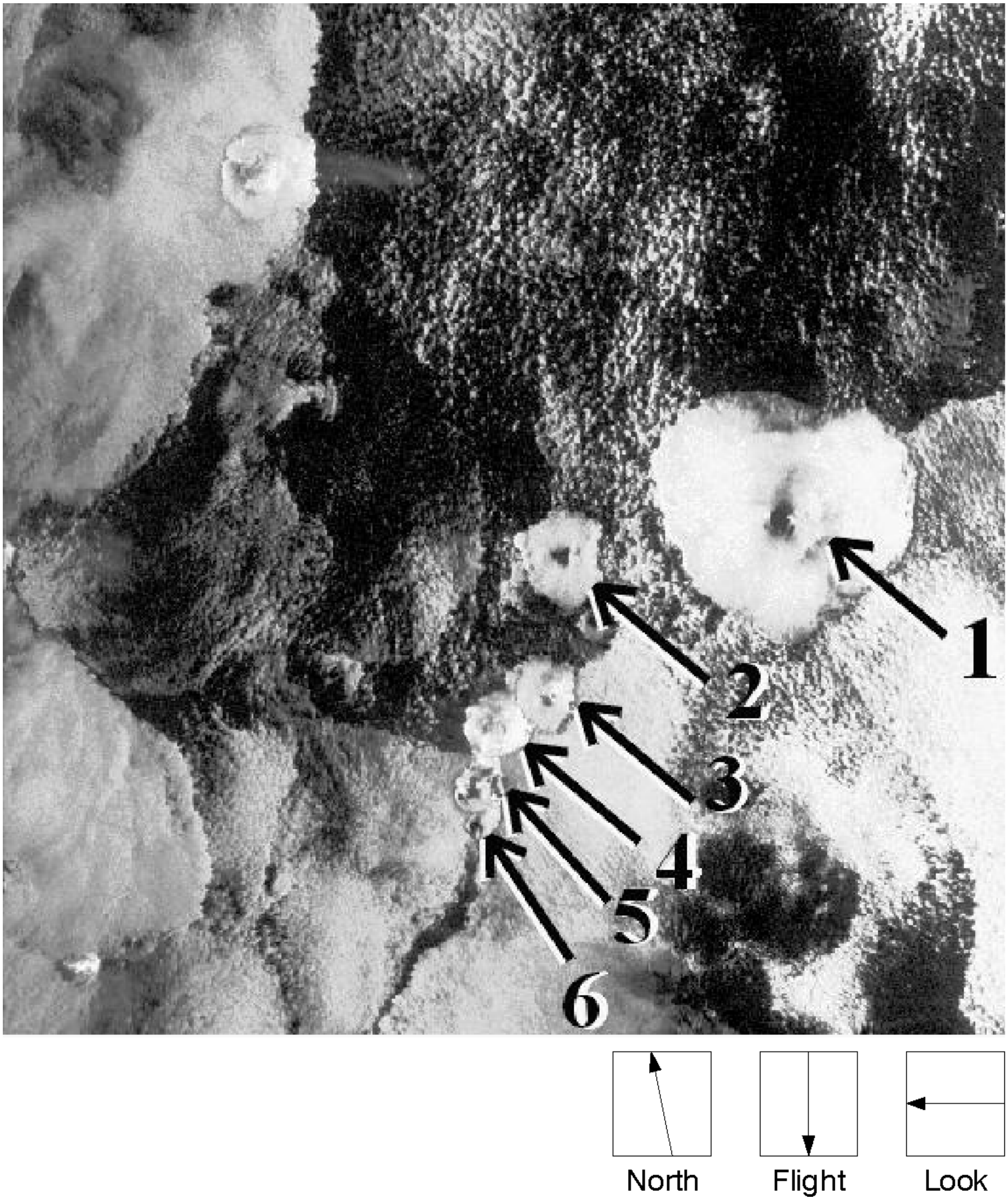

Figure 17.6. ERS-1 (C-band, VV) SAR image acquired on 18 April, 1994, 0342 UTC over the Gulf of Thailand (orbit 14408, frame 3393), showing a string of rain cells, marked "1" to "6", which are in different stages of their life cycles. Rain cell "1" is the oldest and rain cell "6" the youngest one. The imaged area is approximately 100 km × 100 km, center location 10°39'N, 100°49'E. ©ESA 1994

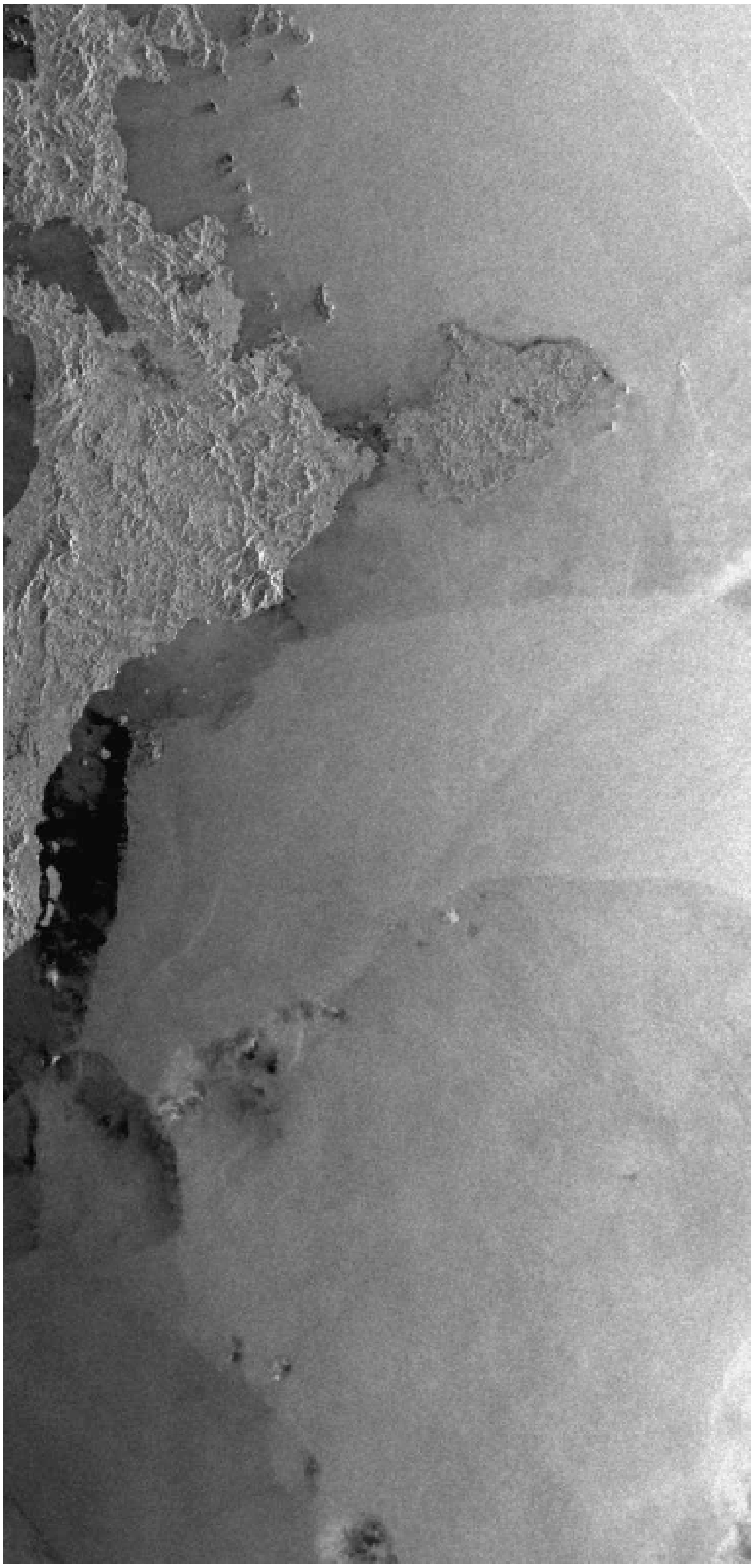

Figure 17.7. ERS-2 (C-band, VV) SAR image acquired on 15 December 1999, 0226 UTC over the Sulu Sea near Palawan Island, Philippines (orbit 24320, frames 3393-3411), showing rain cells without a pronounced downdraft pattern. The imaged area is approximately 200 km × 100 km, center location 10°08’N, 119°10’E. ©ESA 1999

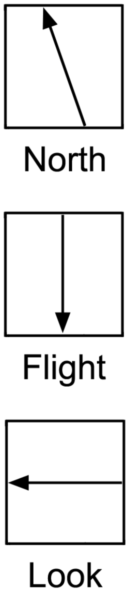

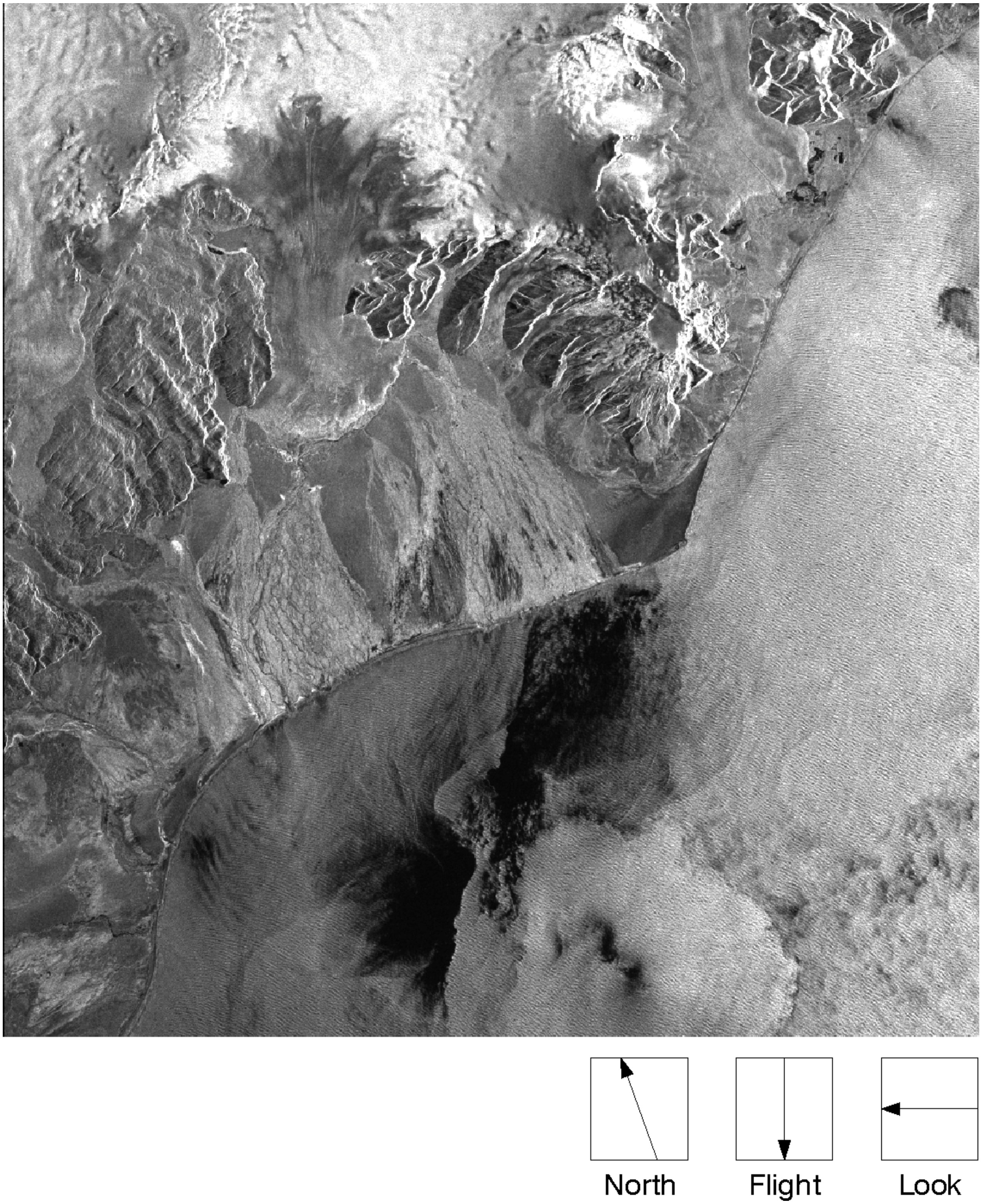

Figure 17.8. ERS-1 (C-band, VV) SAR image, acquired on 7 November, 1996, at 1223 UTC over the south coast and coastal waters of Iceland (Orbit 8108, Frame 2313), showing a large rain cell. The imaged area is approximately 100 × 100 km, center location 63°53'N, 17°03'W.

waves are damped by impinging raindrops. In the high-resolution version of this ERS SAR image (not shown here), swell is visible almost everywhere in the sea portion of the image, even inside the area of the radially spreading downdraft of the rain cell. The reason for this is that, unlike short water waves (Bragg waves), the long water waves (wavelength of the order of 100 m and more) are hardly affected by the local wind field.

Figure 17.9 shows an area of the Gulf of Mexico imaged simultaneously at L, C, and X-band (left to right), at VV, HH, and HV polarizations (top to bottom), by SIR-C/X-SAR on 17 April 1994, 0830 UTC. The strong dependence of the radar signatures on the radar frequency is apparent in these images. The areas marked "a" in the VV polarization L- and C-band images appear dark at L-band and bright at C-band, which implies that at these locations the impinging rain drops damp the L-band Bragg waves (wavelength 21.5 cm) and, at the same time, enhance the C-band Bragg waves (wavelength 5.3cm). The area marked "b" in the X-band image is dark only at X-band, which we interpret as the "shadow" of a rain cell caused by the attenuation of the X-band waves by the hydrometeors in the atmosphere. The area marked "c" is bright in all three VV polarization images; thus, it must be caused by enhanced wind speed. Note that in Figure 17.9, no circular or elliptic radar signatures of spreading downdrafts are visible. This is because, in this case, an isolated rain cell is not imaged, but rather a cluster of irregularly shaped rain cells located along a marked air mass boundary (a cold front, according to the weather chart). The HH polarization C and L-band images (second row) look almost identical to the corresponding images at VV polarization. Furthermore, the VV, HH, and HV images at L-band look almost identical. In contrast, the HV polarization C-band image looks remarkably different from all others. It shows very bright areas where the L-band images show dark areas caused by the damping of the L-band Bragg waves by the rain-induced turbulence.

Similar to Figure 17.9, the strong dependence of rain signatures on radar frequencies is visible in Figure 17.10. Figure 17.10 shows an area of the Northern Straits of Malacca near Penang, Malaysia, imaged simultaneously at L-, C-, and X-band (left to right) at VV, HH, and HV polarizations (top to bottom) by SIR-C/X-SAR on 17 April 1994, 1847 UTC. At L- and C-band, the HH and VV polarization (co-polarization) images are almost identical, but the C-band, HV polarization (cross-polarization) image is distinctly different. While the co-polarization images show two adjacent, almost circular rain cells mainly characterized by the radar signature of the spreading downdraft with a sharp edge (gust front), the cross-polarization image does not show this radar signature as clearly. Instead, it shows patches of strongly enhanced radar backscatter inside the area of the spreading downdraft. This strong enhancement of radar backscatter in rain cells has been regularly observed in cross-polarized C-band SAR images. It has been shown that this effect is not primarily caused by volume scattering by rain drops in the atmosphere, but rather by surface scattering [*Melsheimer et al.*, 1998]. Bragg scattering alone cannot explain the strong enhancement of the radar backscatter. Other backscattering mechanisms must contribute to the enhancement, such as scattering at cavities, crowns, stalks, and secondary drops generated by the raindrops impinging onto the sea surface. This is a topic of ongoing research [*Braun et al.*, 2002]. Note that in contrast to C-band images, L-band images of rain cells over the sea do not show any significant difference between the different polarimetric channels. In view of these observations, the C- and X-band cross-polarization channels seem to be best suited for detecting rain over water surfaces with SAR.

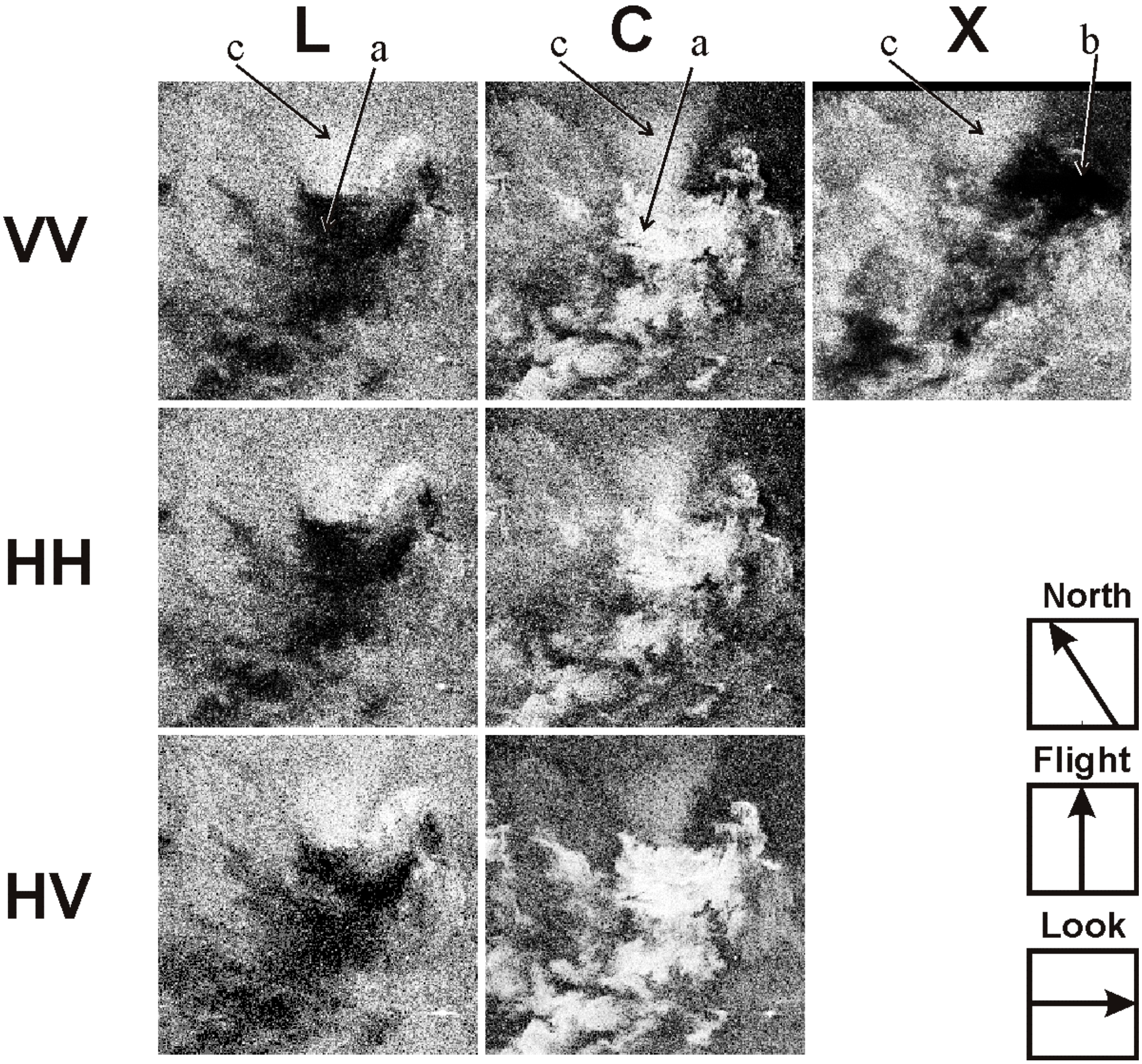

Figure 17.9. SIR-C/X-SAR images acquired on 17 April 1994, 0830 UTC (Data take 129.1) over the Gulf of Mexico, simultaneously at L-, C-, and X-band (left to right) and at different polarizations (top to bottom). A cluster of irregularly shaped rain cells is visible. The areas marked “a” in the VV polarization L- and C-band images are dark at L band (Bragg waves are damped by impinging rain drops), but bright at C band (Bragg waves are enhanced by impinging rain drops). The area marked “b” in the X-band image should be dark only in the X-band image (“shadow” of a rain cell, i.e. the radar beam is attenuated by raindrops in the atmosphere). Area marked “c” is bright in all three VV polarization images (caused by enhanced wind speed due to the downdraft). Each imaged area covers approximately 12 km × 12 km, center location 18°33’N, 93°07’W.

17.4 Conclusion

Rainfall in the form of convective rain (i.e., rain cells) becomes visible in SAR images primarily by three physical processes. The first two processes are surface scattering caused by the modification of the sea surface roughness by (1) impinging rain drops on the water surface and (2) wind gusts (spreading downdrafts) associated with rain cells. The third process is the

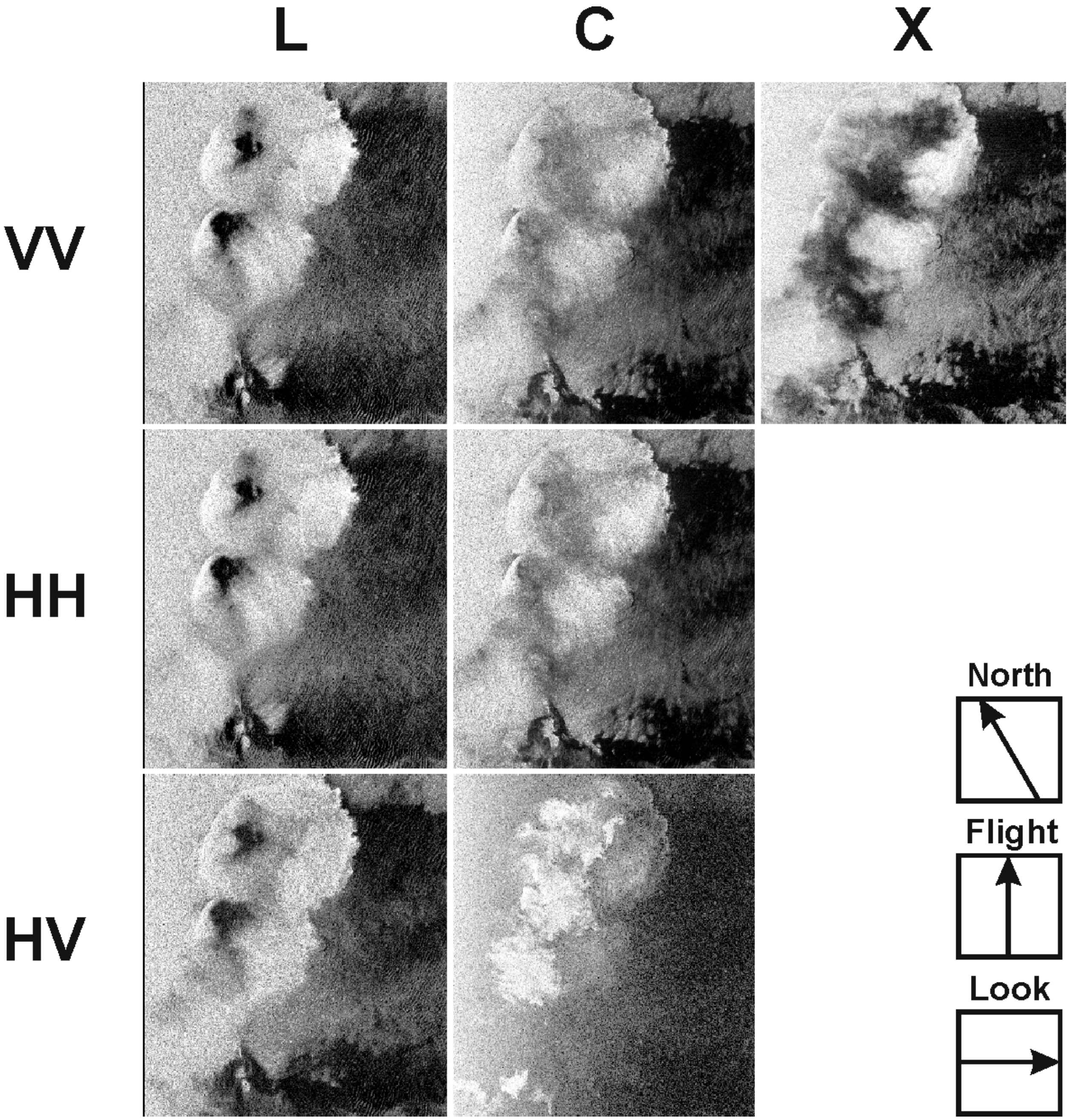

Figure 17.10. SIR-C/X-SAR images acquired on 17 April 1994, 1847 UTC (Data take 136.0) over the Northern Straits of Malacca near Penang, Malaysia. The 7 images were acquired simultaneously at L-, C- and X-band (left to right) and at different polarizations (top to bottom). They show two adjacent rain cells. Each imaged area covers approximately 16 km × 18 km, center location 4°56'N, 100°12'E.

interaction of raindrops in the atmosphere with the radar beam. The first and the third of these processes show a strong dependence on radar frequency and polarization. Therefore, on radar images acquired over the ocean, radar signatures of rain cells can look quite dissimilar at different radar frequencies and polarizations.

17.5 References

Atlas, D., 1994a: Footprints of storms on the sea: A view from spaceborne synthetic aperture radar. *J. Geophys. Res.,* **99**, 7961–7969.

——, 1994b: Origin of storm footprints on the sea seen by synthetic aperture radar. *Science,* **266**, 1364–1366.

——, and P. Black, 1994: The evolution of convective storms from their footprints on the sea as viewed by synthetic aperture radar from space. *Bull. Amer. Meteor. Soc.,* **75**, 1183–1190.

Barry, R. G., and R. C. Chorley, 1987: *Atmosphere, Weather and Climate*. 5th ed. Methuen, 460 pp.

Bliven, L., P. W. Sobieski, and C. Craeye, 1997: Rain generated ring-waves: Measurements and modelling for remote sensing. *Int. J. Remote Sens.,* **18**, 221–228.

Braun, N., M. Gade, and P. A. Lange, 2002: The effect of artificial rain on wave spectra and multi-polarisation X band radar backscatter. *Int. J. Remote Sens.,* **23**, 4305–4322.

Cotton, W. R., and R. A. Anthes, 1989: *Storm and Cloud Dynamics*. Academic, 883 pp.

Craeye, C., P. W. Sobieski, and L. F. Bliven, 1997: Scattering by artificial wind and rain roughened water surfaces at oblique incidences. *Int. J. Remote Sens.,* **18**, 2241–2246.

Doviak, R. J., and D. S. Zrnic, 1993: *Doppler Radar and Weather Observations*. 2d ed. Academic, 562 pp.

Fu, L.-L., and B. Holt, 1982: Seasat views oceans and sea ice with synthetic aperture radar. Jet Propulsion Laboratory Publ. 81-120, 200 pp.

Houze, R. A., Jr., 1997: Stratiform precipitation in regions of convection: A meteorological paradox? *Bull. Amer. Meteor. Soc.,* **78**, 2179–2196.

Iguchi, T., D. Atlas, K. Okamoto, and A. Sumi, 1995: Footprints of storms on the sea in the JERS-1 SAR image. *IEICE Trans. Fundam. Electron. Commun. Comput. Sci.,* **78B**, 1580–1584.

Jameson, A. R., F. K. Li, S. L. Durden, Z. S. Haddad, B. Holt, T. Fogarty, E. Im, and R. K. Moore, 1997: SIR-C/X-SAR observations of rain storms. *Remote Sens. Environ.,* **59**, 267–279.

Kummerow, C., W. Barnes, T. Kozu, J. Shiue, and J. Simpson, 1998: The tropical rainfall measuring mission (TRMM) sensor package. *J. Atmos. Oceanic Technol.,* **15**, 809–817.

Lichtenegger, J., 1996: ERS-1 SAR images: Mirror of thunderstorms. *Eur. Space Agency Earth Obs. Quart.,* **53**, 7–9.

Lin, I.-I., W. Alpers, V. Khoo, H. Lim, T. K. Lim, and D. Kasilingam, 2001: An ERS-1 synthetic aperture radar image of a tropical squall line compared with weather radar data. *IEEE Trans. Geosci. Remote Sens.,* **39**, 937–945.

Melsheimer, C., W. Alpers, and M. Gade, 1998: Investigation of multifrequency/multi-polarization radar signatures of rain cells over the ocean using SIR-C/X-SAR data. *J. Geophys. Res.,* **103**, 18 867–18 884.

——, ——, and ——, 2001: Simultaneous observations of rain cells over the ocean by the synthetic aperture radar aboard the ERS satellites and by surface-based weather radars. *J. Geophys. Res.,* **106** (C3), 4665–4678.

Mitnik, L. M., 1992: Mesoscale coherent structures in the surface wind field during cold air outbreaks over the eastern seas from the satellite side looking radar. *La mer,* **30**, 297–314.

Moore, R. K., Y. S. Yu, A. K. Fung, D. Kaneko, G. J. Dome, and R. E. Werp, 1979: Preliminary study of rain effects on radar scattering from water surfaces. *IEEE J. Oceanic Eng.,* **4**, 30–31.

——, A. Mogili, Y. Fang, B. Beh, and A. Ahamad, 1997: Rain measurement with SIR-C/X-SAR. *Remote Sens. Environ.,* **59***,* 280–293.

Nystuen, J., 1990: A note on the attenuation of surface gravity waves by rainfall. *J. Geophys. Res.,* **95**, 18 353–18 355.

Salby, M. L., 1996: *Fundamentals of Atmospheric Physics*. Academic, 627 pp.

Sauvageot, A., 1991: *Radar Meteorolog*y. Artech House, 384 pp.

Simpson, J., C. Kummerow, W.-K. Tao, and R. F. Adler, 1996: On the Tropical Rainfall Measuring Mission (TRMM). *Meteor. Atmos. Phys.,* **60**, 19–36.

Tournadre, J., 1998: Determination of rain cell characteristics from the analysis of TOPEX altimeter echo waveforms. *J. Atmos. Oceanic Technol.,* **15**, 387–406.

——, and J. C. Morland, 1997: The effects of rain on TOPEX/Poseidon altimeter data. *IEEE Trans. Geosci. Remote Sens.,* **35**, 1117–1135.

Tsimplis, M., 1992: The effect of rain in calming the sea. *J. Phys. Oceanogr.,* **22***,* 404–412.

Valenzuela, G. R., 1978: Theories for the interaction of electromagnetic and ocean waves—A review. *Bound.- Layer Meteor.,* **13***,* 61–85.